8-1-2013

Reducing Radiation Dose to the Female Breast during CT Coronary Angiography: A Simulation Study Comparing Breast Shielding, Angular Tube Current Modulation, Reduced kV, and Partial Angle Protocols Using an Unknown-location Signal-detectability Metric

Franco Rupcich
Marquette University, franco.rupcich@marquette.edu

Andreu Badal
US Food and Drug Administration

Lucretiu M. Popescu
US Food and Drug Administration

Iacovos Kyprianou
US Food and Drug Administration

Taly Gilat Schmidt
Marquette University, tal.gilat-schmidt@marquette.edu

Accepted version. *Medical Physics*, Vol. 40, No. 8 (August 2013): 081921:1-14. DOI.

Medical Physics, Vol. 40, No. 8 (August 2013): 081921:1-14. DOI.

Reducing radiation dose to the female breast during CT coronary angiography: A simulation study comparing breast shielding, angular tube current modulation, reduced kV, and partial angle protocols using an unknown-location signal-detectability metric

Franco Rupcich
Department of Biomedical Engineering, Marquette University, Milwaukee, Wisconsin 53233

Andreu Badal
Center for Devices and Radiological Health, US Food and Drug Administration, Silver Spring, Maryland 20905

Lucretiu M. Popescu
Center for Devices and Radiological Health, US Food and Drug Administration, Silver Spring, Maryland 20905

Iacovos Kyprianou
Center for Devices and Radiological Health, US Food and Drug Administration, Silver Spring, Maryland 20905

Taly Gilat Schmidt
Department of Biomedical Engineering, Marquette University, Milwaukee, Wisconsin 53233

Keywords

Dosimetry/exposure assessment; ; Angiography; Contrast; Noise; Computed tomography; cardiology; computerised tomography; dosimetry; lung; medical image processing; phantoms; CT dose; breast dose; CT image quality; signal detectability; Computerised tomographs; Digital computing or data processing equipment or methods, specially adapted for specific applications; Image data processing or generation, in general; Medical imaging; Lungs; Medical image noise; Medical image quality; Computed tomography; Dosimetry; Photons; Image quality assessment; Medical image contrast; Cancer

Funding Information

- NSF. Grant Number: OCI-0923037
- NSF. Grant Number: CBET-0521602

Abstract

Purpose:

The authors compared the performance of five protocols intended to reduce dose to the breast during computed tomography (CT) coronary angiography scans using a model observer unknown-location signal-detectability metric.

Methods:

The authors simulated CT images of an anthropomorphic female thorax phantom for a 120 kV reference protocol and five “dose reduction” protocols intended to reduce dose to the breast: 120 kV partial angle (posteriorly centered), 120 kV tube-current modulated (TCM), 120 kV with shielded breasts, 80 kV, and 80 kV partial angle (posteriorly centered). Two image quality tasks were investigated: the detection and localization of 4-mm, 3.25 mg/ml and 1-mm, 6.0 mg/ml iodine contrast signals randomly located in the heart region. For each protocol, the authors plotted the signal detectability, as quantified by the area under the exponentially transformed free response characteristic curve estimator ($\hat{A}_{\mathrm{FE}}$), as well as noise and contrast-to-noise ratio (CNR) versus breast and lung dose. In addition, the authors quantified each protocol's dose performance as the percent difference in dose relative to the reference protocol achieved while maintaining equivalent $\hat{A}_{\mathrm{FE}}$.

Results:

For the 4-mm signal-size task, the 80 kV full scan and 80 kV partial angle protocols decreased dose to the breast (80.5% and 85.3%, respectively) and lung (80.5% and 76.7%, respectively) with $\hat{A}_{\mathrm{FE}}$= 0.96, but also resulted in an approximate three-fold increase in image noise. The 120 kV partial protocol reduced dose to the breast (17.6%) at the expense of increased lung dose (25.3%). The TCM algorithm decreased dose to the breast (6.0%) and lung (10.4%). Breast shielding increased breast dose (67.8%) and lung dose (103.4%). The 80 kV and 80 kV partial protocols demonstrated greater dose reductions for the 4-mm task than for the 1-mm task, and the shielded protocol showed a larger increase in dose for the 4-mm task than for the 1-mm task. In general, the CNR curves indicate a similar relative ranking of protocol performance as the corresponding $\hat{A}_{\mathrm{FE}}$ curves, however, the CNR metric overestimated the performance of the shielded protocol for both tasks, leading to corresponding underestimates in the relative dose increases compared to those obtained when using the $\hat{A}_{\mathrm{FE}}$ metric.

Conclusions:

The 80 kV and 80 kV partial angle protocols demonstrated the greatest reduction to breast and lung dose, however, the subsequent increase in image noise may be deemed clinically unacceptable. Tube output for these protocols can be adjusted to achieve a more desirable noise level with lesser breast dose savings. Breast shielding increased breast and lung dose when maintaining equivalent $\hat{A}_{\mathrm{FE}}$. The results demonstrated that comparisons of dose performance depend on both the image quality metric and the specific task, and that CNR may not be a reliable metric of signal detectability.

I. INTRODUCTION

Over the last several decades, computed tomography (CT) has become a common tool in medicine. As of 2010, it is estimated that approximately 10% of the United States population undergoes a CT scan each year, with a total of 75 million scans being conducted (half of which are performed on women). Further, the number of scans performed continues to increase each year by approximately 10%.[1] The health benefits of CT in the screening, diagnosis, and treatment of disease cannot be overstated. Still, CT scans impart ionizing radiation upon the patient. The prevailing (albeit debated[2,3]) theory regarding ionizing radiation dose and cancer incidence is referred to as the *linear no-threshold (LNT)* model and is supported by the National Commission on Radiological Protection (NCRP).[4] The LNT model assumes *the risk of cancer incidence from exposure to low levels of ionizing radiation increases linearly with cumulative dose, and there is no threshold dose below which the magnitude of the risk is zero*.[5] Thus, while the levels of ionizing radiation dose imparted during CT procedures are fairly low (<100 mSv), the increasing number of procedures being performed each year, as well as the prevailing assumption that risk is proportional to the cumulative dose received coupled with the fact that many patients receive multiple scans, has motivated a concerted effort among clinicians, radiologists, researchers, government agencies, policy makers, and manufacturers of radiologic imaging systems to reduce the radiation dose to patients as low as reasonably achievable.

Although no large-scale epidemiological study has established specific levels of cancer risk associated with CT scans per se for adults (one retrospective cohort study has been published for children undergoing brain CT scans[6]), the comprehensive Biological Effects of Ionizing Radiation (BEIR) VII Phase 2 report has established risk projections and models in general for radiation-attributable cancer incidence resulting from exposure to low levels of ionizing radiation (similar to those procured during a typical CT examination), which have been estimated largely on the basis of radiation epidemiology studies of atomic bomb survivors, and to a lesser extent, populations living near nuclear accident sites and workers with occupational exposures.[5] The report further indicates that women exposed to radiation at any age suffer a higher lifetime attributable risk (LAR) of general cancer incidence and mortality than men exposed at the same age. Using epidemiological risk models proposed in the BEIR VII report, Einstein *et al.* have estimated the LAR of general cancer incidence associated with a single retrospectively gated CT coronary angiography (CTCA) scan to be 1 in 143 for a 20-year-old female and 1 in 284 for a 40-year-old female, with the primary contributors to the overall risk being breast and lung cancer specifically.[7] Using these same risk models, Smith-Bindman *et al.* estimated the LAR of general cancer incidence associated with a single CTCA scan to be 1 in 150 for a 20-year-old female and 1 in 270 for a 40-year-old female, again with the primary contributors to the overall risk being breast and lung cancer.[8]

Considering the evidence of higher breast cancer incidence following low levels of radiation exposure, recommendations from the International Commission of Radiation Protection (ICRP) have increased the tissue weighting factor of the breast such that it is considered one of the most radiosensitive organs.[9] This recommendation, along with the data from the above mentioned studies, has motivated clinicians and researchers to investigate and optimize methods for reducing breast dose while maintaining diagnostically suitable image quality during CT examinations in which the breast is directly irradiated.

Several studies have reported reduction in adult female breast dose during chest CT scans using dose reduction techniques such as angular tube current modulation (10%–64% reduction in breast dose),[10–13] partial-angle

scanning (50%),[12] and reduced x-ray kV (27%–50%).[10,14] Breast shielding has also been shown to reduce breast dose (29%–57%),[10–12,15–17] although it has been suggested that similar dose savings can be achieved more efficiently via global tube-current reduction.[11,12,15] When assessing the resultant image quality, the aforementioned studies performed a subjective analysis[10,15–17] and/or quantified task-independent metrics such as noise (pixel standard deviation) or contrast-to-noise ratio (CNR).[11,12,14,17] In medical diagnostic imaging, image quality must express the effectiveness with which the image can be used for a specific diagnostic task (e.g., detection of a lesion or estimation of the degree of stenosis). Accordingly, the International Commission on Radiological Units (ICRU) recommends the objective assessment of image quality, and more specifically, the use of task-dependent metrics over task-independent metrics, as the latter may not always be directly indicative of the diagnostic performance of the intended task and thus may not fully accurately represent the true "quality" of an image.[18]

The objective assessment of image quality comprises four main elements: the diagnostic task (e.g., detection of an object or estimation of a parameter), a description of the statistical properties of the data (e.g., a set of images from which statistical properties can be derived), the observer (a mathematical model or human that performs the given task), and the figure of merit [a summary metric, such as signal-to-noise ratio (SNR) or area under the relative operating characteristic (ROC) curve (AUC ROC), estimated from the output of the observer that indicates how well the observer performed the given task].[19] For tasks for which the signal location is unknown, which are often more clinically relevant, we can estimate the localization ROC (LROC) curve, which plots the fraction of true positive images with a correctly localized signal versus the fraction of false positive images. The area under the LROC curve, AUC LROC, may then be used as a detectability metric instead of AUC ROC for tasks in which the signal location is unknown.[20] For cases in which there are multiple signals with unknown locations, we may use the free-response operating characteristic (FROC) method, which allows the observer to mark and score all potentially nonoverlapping suspicious locations. The FROC curve plots the ratio of true signals detected versus the average number of false signals reported per image. As such, the FROC graph does not have a well-defined right side limit, and so the area under the FROC curve is undefined and cannot be used as a performance index. Popescu recently introduced an exponential transformation of the FROC curve (EFROC) that maps the infinite interval of the abscissa to a finite one and then shows that the area under the EFROC curve, AUC EFROC, can be used as a signal detectability metric.[21] Moreover, this method is nonparametric in that AUC EFROC is estimated directly from the confidence scores reported by the observer, thereby avoiding the reliance on specific models or assumptions typically required when estimating an area under the curve metric via direct integration under its associated ROC curve.

In general, image quality metrics can be plotted as a function of a physical parameter of the imaging process (e.g., radiation dose) to summarize the effect of that parameter on signal detectability.[18] Such plots can then be obtained for several different imaging systems, reconstruction algorithms, or techniques to determine which ranks the highest with respect to the chosen parameter. For example, a recent study compared CT images reconstructed using filtered back projection to those reconstructed using an iterative algorithm by plotting AUC LROC vs dose (mAs) curves for the two algorithms and observing which produced a higher detectability at a given radiation dose.[22]

The purpose of this model observer study was to compare the signal detectability, as quantified by the AUC EFROC estimator, $\hat{A}_{\mathrm{FE}}$, of several dose reduction techniques over a range of breast dose levels. Because the lung is considered as radiosensitive as the breast[9] and lung dose may be affected by breast dose reduction methods, we further investigated AUC EFROC versus lung dose. We estimated other commonly used image quality metrics, including noise, contrast, and CNR, to assess their relationship to AUC EFROC and determine whether they may serve as accurate predictors of detectability or are sufficient quantifiers of image quality. We studied two tasks—detection and localization of small diameter/high contrast and large diameter/medium contrast signals—to investigate how the dose savings potential may vary depending on the task, where "detection and

localization" refers to the case in which the signal location is unknown, and thus the signal must be both detected and have its location correctly identified.

II. METHODS

II.A. Overview

We simulated CT images of an anthropomorphic female thorax phantom for a 120 kV reference protocol, as well as five "dose reduction" protocols intended to reduce dose to the breast during CTCA acquisitions. For each protocol and two chosen image quality tasks, we calculated a model observer metric, the AUC EFROC estimator, $\hat{A}_{\mathrm{FE}}$, and plotted it versus breast dose to investigate the potential of that protocol to reduce dose to the breast without affecting the image quality as quantified by $\hat{A}_{\mathrm{FE}}$, i.e., the detectability of the signals. Because noise, contrast, and CNR are often used in assessing image quality, we also plotted these metrics against breast dose. We further investigated each of the metrics versus lung dose.

Subsections II B–II H describe in further detail the phantom and task design, CT simulation geometry, and our methods for simulating the images, estimating dose, and calculating $\hat{A}_{\mathrm{FE}}$ for each protocol and task.

II.B. Unknown-location signal-detectability metric ($\hat{A}_{\mathrm{FE}}$) estimation

This study estimated image quality using a task-based procedure that detected signals at unknown locations in the image region of interest (cardiac region). The procedure comprises (1) a signal searching algorithm that produces free response data, i.e., the scores of all suspicious locations (either true or false signals) and their respective location marks, and (2) a nonparametric free response data analysis method.21 The signal searching and the data analysis have been applied as recently presented by Popescu and Myers.23 The signal searching algorithm was initially presented in Popescu and Lewitt.24

For a given (signal-absent or signal-present) image region of interest (ROI), signal detection is performed using a signal search algorithm with two main steps. The first step generates an auxiliary scan image by cross-correlating the image ROI with a series of shifted signal templates. We assume that an image ROI consists of M pixels and is represented in vectorized form by $\mathbf{f}$. A signal template, $\mathbf{w}_i$, consists of M pixels, all with a value of zero except those located within the disk of radius R_t centered at point i, which have a value of one. The value of the scan image at the ith pixel location, z_i is given by Eq. (1):

$$z_i = \Sigma_{i=1}^{\mathrm{M}} \mathbf{w}_i^{\mathrm{T}} \mathbf{f}. \qquad (1)$$

In other words, z_i is the sum of the pixel values within the disk of radius R_t centered at point i, providing a measure of the match between the signal template and the pixels around that location. z_i is the *scan score* for the ith pixel in $\mathbf{f}$, and $\mathbf{z}$ is referred to as the *scan image*. The second step involves marking all suspicious locations of the image. We first determine the maximum scan score of the scan image, $\mathbf{z}$. The scan score is recorded, and the pixels within a disk of radius twice that of the signal radius around this point are masked (i.e., set to zero). This step is then repeated with the remaining unmasked pixels of $\mathbf{z}$ until the local maximum scan score is less than a chosen stopping limit, z_0. The output of this step is a descending list of scan scores for all suspicious locations of the image with a value above z_0.

Using this procedure, we obtain $\{X_i\}$, the scan scores for I true signals present, and $\{Y_j\}$, the scan scores of a total of J false signals retrieved from N signal-absent image ROIs. From these two sets of data, we can estimate AUC EFROC as

$$\hat{A}_{\mathrm{FE}} = \frac{1}{I} \Sigma_{i=1}^{I} e^{-\frac{1}{N}\Sigma_{j=1}^{J} H(Y_j - X_i),} \qquad (2)$$

where $H(k)$, the Heaviside equation, is equal to 1 if $k > 0$; 1/2 if $k = 0$; or 0 if $k < 0$.

The statistical properties of this signal-detectability estimator and its relations with ROC, LROC, and alternative FROC (AFROC) metrics have been studied in detail in Ref. 21. In addition, nonparametric equations for the variance calculations are provided.

II.C. Simulation setup

The ray-tracing and Monte Carlo simulations described in this study were performed with the penEasy_Imaging software package,25,26 which relies on the previously validated PENELOPE Monte Carlo radiation transport routines and material attenuation database.27 The ray-tracing algorithm operates by calculating analytical line integrals from the x-ray point source to each detector pixel to determine the probability of transmission associated with each detector pixel and the material attenuation coefficients along that line. Multiple rays are cast for each pixel and averaged to mitigate possible aliasing effects. The geometric transport routines used for the ray-tracing algorithm are the same as those used for the previously validated PENELOPE Monte Carlo routines.27 As an additional validation, images obtained using ray-tracing were compared with primary-only (i.e., scatter-free) images obtained using the Monte Carlo algorithm, and it was confirmed that the images were equivalent (within the uncertainties inherent in the Monte Carlo estimation). The analytical ray-tracing software can reproduce the image generated by the primary x-ray beam, but it does not model individual interactions and therefore does not model x-ray scatter.

This study used the 0.5 mm voxelized anthropomorphic phantom, Ella, from the Virtual Family,28,29 representing an average-sized 26-year-old female (height: 1.63 m, weight: 58.7 kg). To relax computational memory requirements during simulations, we cropped the phantom to the thorax, measuring 31 by 22 cm in the lateral and anteroposterior directions, respectively, and 30 cm in the axial direction. Topograms of the whole body and cropped phantom are shown in Fig. 1.

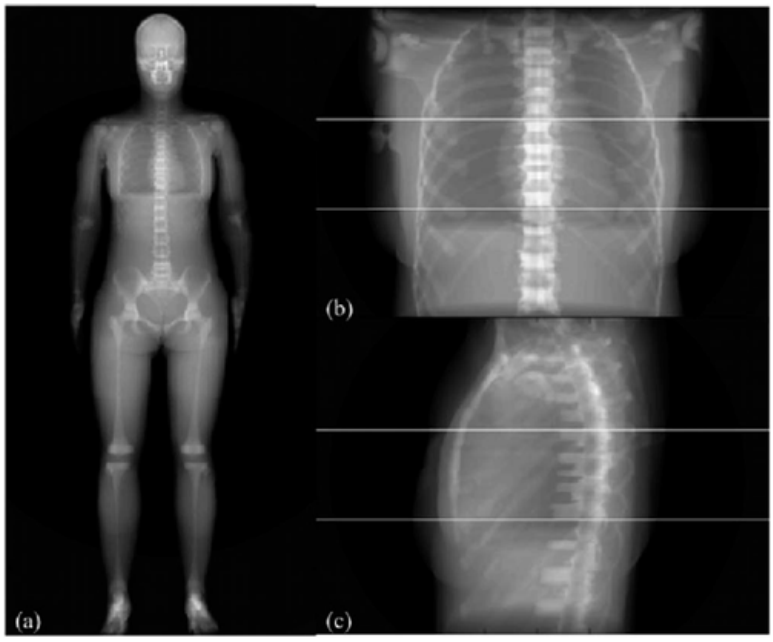

Figure 1
(a) Topogram of the whole body (noncropped) female phantom. (b) Anteroposterior and (c) lateral topograms of the cropped phantom. The scan field-of-view is represented by the space between the white horizontal lines and corresponds to a CTCA scan.

The breast was modeled as two separate parts: an internal glandular mass and an external 1 cm thick surrounding layer of adipose. Thus, voxels representing the internal glandular mass were modeled as 100% glandular tissue, while the surrounding layers of voxels were modeled as 100% adipose. As such, "dose to breast" in the context of this study refers to dose to the 100% glandular material. Voxels representing the following organs/tissues were modeled according to their respective atomic compositions and densities as given by ICRP publication 110:[30] fat (adipose), glandular tissue, blood, cartilage, esophagus, stomach, heart, kidney, liver, muscle, pancreas, skin, spleen, thyroid, and soft tissue. Voxels representing the following organs/tissues were modeled according to their respective atomic compositions and densities as given by Woodard and White:[31] lung (blood filled, 50% inflated, 50% deflated, density: 0.655 g/cm^3), cerebrospinal fluid, and connective tissue. The diaphragm was modeled as muscle. All skeletal voxels were modeled as homogenous bone (density: 1.4 g/cm^3) as given by Cristy and Eckerman.[32]

The image quality tasks were detection and localization of 4-mm, 3.25 mg/ml iodine (≈34 HU contrast at 120 kV) and 1-mm, 6.0 mg/ml iodine (≈55 HU contrast at 120 kV) contrast signals located within the heart region [Fig. 2(a)]. The former task was chosen to approximately represent the uptake of iodine during a CTCA scan, while the latter was chosen to determine if and how task variability may affect potential dose savings. As was explained in Sec. II B, the signal search algorithm and method for calculating $\hat{A}_{\mathrm{FE}}$ require a set of signal-absent ROIs, which were obtained by simulating images of the phantom with no iodine contrast elements present, as well as a set of signal-present ROIs, which were obtained by simulating images of the phantom with either five 1-mm, 6.0 mg/ml [Fig. 2(b)] or five 4-mm, 3.25 mg/ml [Fig. 2(c)] cylindrical iodine contrast elements located in a single axial plane within the heart region.

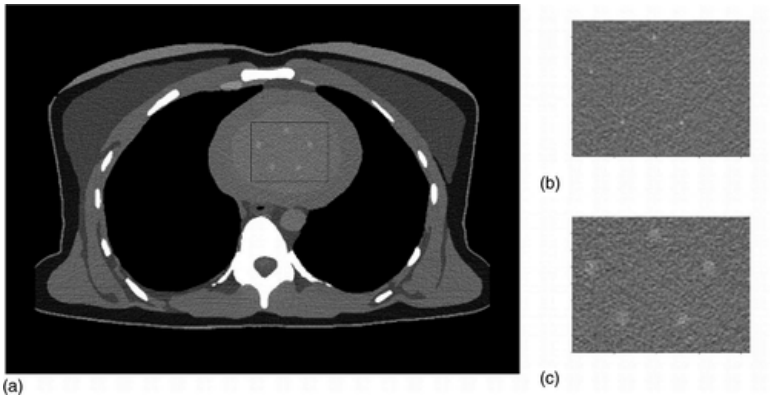

Figure 2
(a) A full field-of-view reconstructed image of the phantom (4-mm, 3.25 mg/ml signal-present). The black box in the heart region indicates the signal search ROI (52.5 × 40 mm^2) used for calculating $\hat{A}_{\mathrm{FE}}$ for both tasks. (b) An example of a signal-present ROI with the 1-mm, 6.0 mg/ml signals. (c) An example of a signal-present ROI with the 4-mm, 3.25 mg/ml signals.

II.D. Simulation geometry

The source-to-detector distance for each simulation was 100 cm, with a source-to-isocenter distance of 50 cm. We modeled a single-rotation stationary cone-beam system with a flat-panel detector, no table translation, and a beam width at isocenter of 8 cm [Figs. 1(b) and 1(c)], which was chosen to represent the scanning capabilities of volumetric CT scanners during CTCA scans.[33,34] We modeled a point source with a fan angle of 53.13°, which was wide enough to cover the entire width of the cropped phantom (44.7 cm FOV). The beam was collimated to exactly cover the surface of the detector. A bowtie filter corresponding to that used for the body protocols of a Siemens AS+ scanner[35] was modeled during all simulations and dose estimations.

II.E. Investigated protocols

We simulated six CT protocols for each of the two tasks, including one reference and five dose reduction protocols:

1. 120 kV (reference)
2. 120 kV partial-angle (tube-current turned off during anteriorly centered 128°)
3. 120 kV angular TCM (proportional to square root of attenuation[36])
4. 80 kV
5. 80 kV partial-angle (tube-current turned off during anteriorly centered 128°)
6. 120 kV breast shielded

Both the 120 kV (HVL, 9.0 mm Al) and 80 kV (HVL, 6.4 mm Al) spectra used in this study were generated using the IPEM Report 78 software[37] (tungsten target, 12° anode angle, 0% voltage ripple, and 6 mm aluminum filtration).

One thousand projections were collected over 360° for the four nonpartial angle protocols: 120 kV, 120 kV TCM, 80 kV, and 120 kV shielded. The two partial-angle protocols reduce direct exposure of the breast by turning off the tube-current during the anteriorly centered 128° (i.e., applying tube-current only during the posteriorly centered 232°);[12] thus only the posteriorly centered 645 projections were collected for these protocols. So-called "organ-based modulation" technology such as XCare (Siemens Healthcare, Germany) reduces the tube-current (≈75%) within a 120° arc and increases tube-current during the remaining 240° of the scan.[11,38–40] We chose a slightly wider arc (128°) during which the tube-current is completely turned off so as to further reduce direct exposure of the breast to radiation from the x-ray source during the anterior angles of the scan (Fig. 3). Lungren *et al.* has shown that many female patients would require a wider arc (at least 175°) to fully encompass the breast tissue.[40] As Fig. 3 demonstrates, this is also true for our female phantom. However, because current technology such as Siemens XCare has a maximum 120° arc, we chose a similar partial-angle for our partial-angle protocols.

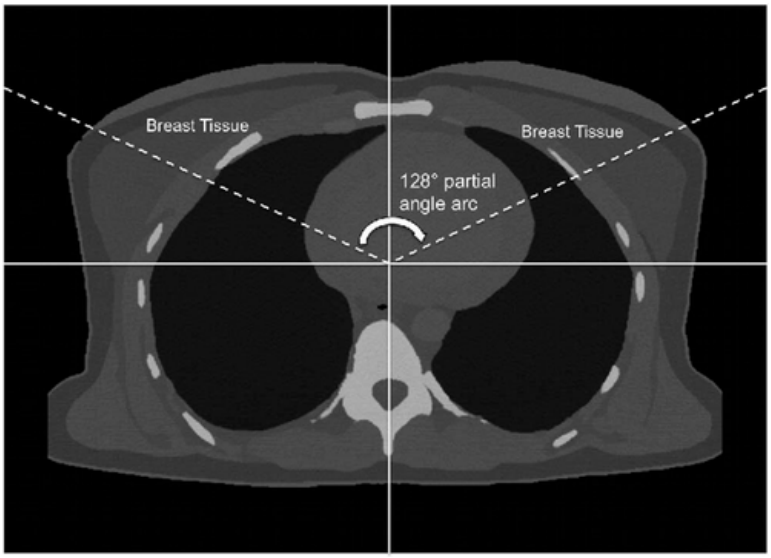

Figure 3
An image of the phantom showing the 128° arc during which the tube current is turned off for the two partial-angle protocols.

For the 120 kV angular TCM protocol, the number of photons emitted from the source (i.e., tube-current) at each projection angle was modulated proportionally to the square root of the attenuation at that angle. This modulation scheme is theoretically optimal with respect to noise (pixel standard deviation) within a homogenous phantom.[36]

For the 120 kV shielded protocol, a 6 mm thick lead shield with density 0.1134 g/cm^3 (1% the actual density of lead) with an approximate length of 42 cm was created using mathematical quadrics and positioned approximately 1 cm above the chest (Fig. 4). Commercially available bismuth shields are typically composed of a proprietary bismuth mixture. It has been previously reported that commonly used 4-ply bismuth-mixture shields have a 0.06 mm lead equivalence (56% attenuation at 120 kVp), noting that lead and bismuth have similar atomic numbers of 82 and 83, respectively.12,16 Thus, we modeled our shield using the abovementioned thickness and density of lead. We did not perform an 80 kV shielded protocol as the combination of the lower energy spectrum and the highly attenuating shield would likely result in unacceptable image quality.

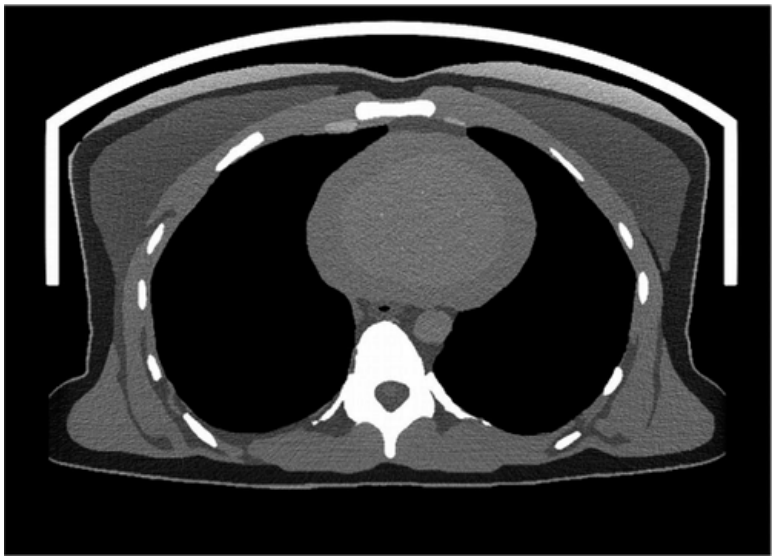

Figure 4
An image of the phantom with the breast shield.

II.F. Dose estimation

We used our previously proposed dose database41 to estimate protocol-specific "dose conversion factors," which quantified the breast dose and lung dose per photon emitted from the source for each protocol. Because our dose database cannot model shielded scans, we performed Monte Carlo simulations (following the methods of Rupcich *et al.*41) of the female phantom with the shield described in Sec. II E to estimate the dose per photon emitted from the source for the shielded protocol. These conversion factors were then multiplied by the number of photons emitted from the source during ray-tracing simulations to calculate the breast and lung dose.

II.G. Image generation

Ray-traced images with added Poisson noise were generated for each of the studied protocols assuming the scan parameters described in Sec. II E. CT projection data were simulated for the 4-mm, 3.25 mg/ml task for the reference 120 kV protocol at 14 different breast dose levels ranging from approximately 1–81 mGy, corresponding to a number of photons emitted from the source ranging from approximately 4.0×10^9 to 4.0×10^{11}. Similarly, projection data were simulated for the 1-mm, 6.0 mg/ml task for 18 different breast dose levels ranging from approximately 1–254 mGy, corresponding to a number of photons emitted from the source ranging from approximately 5.7×10^9 to 1.3×10^{12}. These photon numbers were selected empirically to provide corresponding values of $\hat{A}_{\mathrm{FE}}$ that spanned the full performance range (i.e., from very poor to virtually certain detectability). Note that a linear conversion factor could be applied to convert the number of photons to approximate mAs values. However, mAs values were not reported because the relationship between mAs and

tube output is scanner specific. Thus, we only report the breast and lung doses corresponding to the numbers of simulated photons. The breast dose resulting from the reference 120 kV protocol for each simulated number of photons was calculated by multiplying the breast dose conversion factor of the reference protocol (Sec. II F) by the number of photons emitted from the source. Similarly, each of the five studied breast dose reduction protocols were then simulated at the 14 (4-mm, 3.25 mg/ml task) or 18 (1-mm, 6.0 mg/ml task) different breast dose levels. The corresponding lung dose at each of these data points was then determined by multiplying the lung dose conversion factor for each protocol by the number of photons emitted from the source. The simulated CT data were reconstructed using filtered back projection onto 0.25 mm^2 pixels. The partial-scan data were reconstructed using filtered backprojection with Parker weighting.[42] A water beam-hardening correction algorithm was implemented to reduce cupping artifacts.[43]

II.H. Assessment of dose and image quality

We assessed task-based objective image quality by comparing $\hat{A}_{\mathrm{FE}}$ vs dose curves of the studied protocols. We also estimated the noise, contrast, and CNR for each protocol.

II.H.1. Signal detectability, $\hat{A}_{\mathrm{FE}}$

For this study, the signal search area for signal-present and signal-absent images for both tasks was a two-dimensional 52.5 × 40 mm^2 ROI located in one axial plane inside the heart [Fig. 2(a)]. The radius of the disk within each 2D signal template was one pixel larger than that of the signal, i.e., R_t = 0.75 mm for the 1-mm diameter signal and R_t = 2.25 mm for the 4-mm diameter signal. To assure low statistical uncertainty in $\hat{A}_{\mathrm{FE}}$, we used a total of 40 signal-present and signal-absent ROIs for the 1-mm signal task, and 70 signal-present and signal-absent ROIs for the 4-mm task. The threshold, z_0, was chosen so that a large enough number of suspicious locations per image were retrieved.

The AUC EFROC estimator is scalable with the search area size. For homogeneous regions, $\hat{A}_{\mathrm{FE}}$ can be scaled relative to a given reference image size, Ω, by setting $N = \Omega_T/\Omega$, where Ω_T is the total searched area for false signals (i.e., the signal search area times the number of signal-absent images). We used Ω = 3200 mm^2 (e.g., 56.6 × 56.6 mm^2) for the 4-mm, 3.25 mg/ml task and Ω = 312.5 mm^2 (e.g., 17.7 × 17.7 mm ^{2}) for the 1-mm, 6.0 mg/ml task.

AUC LROC is used for tasks involving detection and localization of a single signal. In theory, the AUC LROC estimator, $\hat{A}_{\mathrm{L}}$is equivalent to $\hat{A}_{\mathrm{FE}}$ when the latter is expressed for a search area size that is twice the size of the ROI area used in estimating the former.[21] Thus, for the 4-mm task, our values of $\hat{A}_{\mathrm{FE}}$ for a search area size of 3200 mm^2 are equivalent to corresponding $\hat{A}_{\mathrm{L}}$values for an ROI size of 1600 mm^2 (e.g., 40 × 40 mm^2). Similarly, for the 1-mm task, the search area size of 312.5 mm^2 represents an A_{L} ROI size of 15.7 mm^2 (e.g., 12.5 × 12.5 mm^2).

$\hat{A}_{\mathrm{FE}}$ was calculated for each CT protocol for both tasks from images simulated at multiple equivalent breast dose levels. It is important to quantify the effects of the different CT protocols on dose to organs other than the breast. The lung dose was calculated for each protocol at each breast dose level by multiplying the lung dose conversion factors described in Sec. II F by the number of simulated photons emitted from the source. We investigated lung dose because of its high radiosensitivity (equivalent to that of the breast) and presence throughout the thorax for the chosen scan geometry.

II.H.2. Dose reduction at equivalent $\hat{A}_{\mathrm{FE}}$

The percent change in dose for a given protocol (relative to the reference protocol) was estimated by comparing the doses required to achieve a specified $\hat{A}_{\mathrm{FE}}$. An $\hat{A}_{\mathrm{FE}}$value too far outside the operating range of a real imaging system could produce misleading results. We chose a value of 0.96, which is close to a clinically realistic AUC ROC operating point for systems performing multislice CTCA.[44] Thus, for any given “dose reduction” protocol,

we quantified dose performance as the percent difference in dose relative to the reference protocol achieved while maintaining an $\hat{A}_{\mathrm{FE}}$ of 0.96.

For a given protocol and signal size, we randomly sampled 500 $\hat{A}_{\mathrm{FE}}$vs breast dose curves assuming a normal distribution of $\hat{A}_{\mathrm{FE}}$ at each dose value with the mean and variance of $\hat{A}_{\mathrm{FE}}$ as estimated in Sec. ???. Each realization of the $\hat{A}_{\mathrm{FE}}$ vs breast dose curve was interpolated to estimate the breast dose at $\hat{A}_{\mathrm{FE}}$ =0.96. This resulted in 500 estimates of breast dose at $\hat{A}_{\mathrm{FE}} = 0.96$, from which we calculated the mean breast dose, $\widehat{D}$, and variance, $\hat{\sigma}^2$ The percent change in breast dose for protocol *p* relative to the reference protocol, *ref*, was estimated using Eq. (3):

$$\%\ \text{change in dose} = \frac{\widehat{D}_{\mathrm{p}} - \widehat{D}_{\mathrm{ref}}}{\widehat{D}_{\mathrm{ref}}} \cdot 100\% \qquad (3)$$

The variance in the estimate of a percent change in dose was calculated by propagating $\hat{\sigma}^2$through Eq. (3). The percent change in lung dose for each protocol was calculated similarly.

II.H.3. Pixel noise, contrast, and contrast-to-noise ratio estimation

Noise was estimated for each protocol by taking the pixel standard deviation of background ROIs across all images collected for that protocol for the given task. Contrast was estimated by calculating the absolute value of the difference between the mean across all images of a background ROI and the mean across all images of a ROI within a signal. CNR was then calculated by dividing the contrast by the noise. Similar to $\hat{A}_{\mathrm{FE}}$, noise and CNR were also plotted against breast dose and lung dose. The pixel noise, contrast, and CNR associated with an $\hat{A}_{\mathrm{FE}}$of 0.96 for protocol p were obtained by interpolating the noise, contrast, and CNR vs dose curves, respectively, for $\widehat{D}_{\mathrm{p}}$.

III. RESULTS

Figure 5 plots $\hat{A}_{\mathrm{FE}}$ versus breast dose and lung dose for each of the studied protocols and for both tasks. Figures 5(a) and 5(c) indicate that for both tasks, the 80 kV, 80 kV partial, and 120 kV partial protocols exhibited better signal detectability than the reference protocol at a given breast dose, while the shielded protocol exhibited poorer detectability. The TCM protocol exhibited comparable performance to the reference protocol. Further, at a given breast dose, performance was better for a partial scan than for a full scan (at the same kV).

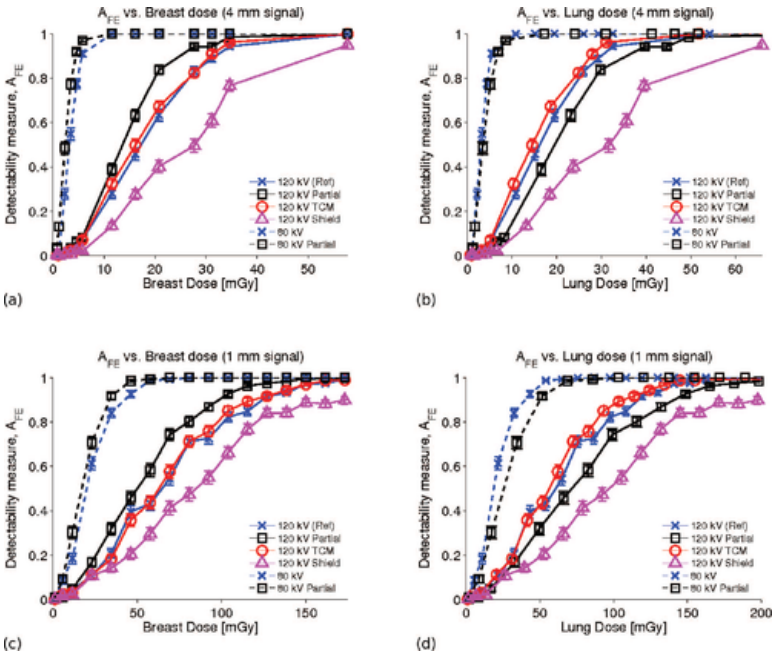

Figure 5

$\hat{A}_{\mathrm{FE}}$ vs (a) breast dose and (b) lung dose for the 4-mm, 3.25 mg/ml signals. $\hat{A}_{\mathrm{FE}}$ vs (c) breast dose and (d) lung dose for the 1-mm, 6.0 mg/ml signals. Note that error bars are present in the plots and represent one standard deviation in either direction, but in most cases are too small to see over the plot markers.

Figures 5(b) and 5(d) indicate that for both tasks, the 80 kV and 80 kV partial protocols exhibited better performance per lung dose than the reference protocol. At a given lung dose, the TCM protocol exhibited comparable performance to the reference protocol, while the 120 kV partial and shielded protocols exhibited poorer performance. Unlike the $\hat{A}_{\mathrm{FE}}$ vs breast dose curves, the $\hat{A}_{\mathrm{FE}}$ vs lung dose curves indicate better performance for full scans than for partial scans (at the same kV). In general, 80 kV protocols showed better performance per breast dose or lung dose than 120 kV protocols.

We note that for the 4-mm, 3.25 mg/ml task, which represents the clinical case of iodine uptake within a coronary vessel, the range of breast doses in Fig. 5(a) is reasonable considering the typical breast doses estimated for a CTCA protocol.45 On the other hand, for the 1-mm, 6.0 mg/ml task, which is not necessarily representative of a typical CTCA task due to its small signal size and high contrast, relatively higher doses are required to span the full performance range [Fig. 5(c)], implying a higher level of difficulty in terms of signal detectability than the 4-mm, 3.25 mg/ml task.

Figure 6 plots the noise standard deviation versus breast dose and lung dose for each of the studied protocols. Because the signals are small, it is safe to assume the noise is not dependent on the signal. Thus, the following results apply for both the 4 and 1-mm signal sizes. Figure 6(a) indicates higher noise per breast dose for the 80 kV, 80 kV partial, and shielded protocols, and lower noise per breast dose for the 120 kV partial protocol, relative to the reference protocol. The TCM protocol showed comparable noise per breast dose to the reference scan. Figure 6(b) shows relatively higher noise per lung dose for all protocols except the TCM protocol, which exhibited comparable noise per lung dose to the reference protocol. Noise per breast dose was lower for a full scan than for a partial scan (at the same kV), while the opposite was true for noise per lung dose. In general, 80 kV protocols yielded higher noise per breast dose or lung dose than 120 kV protocols.

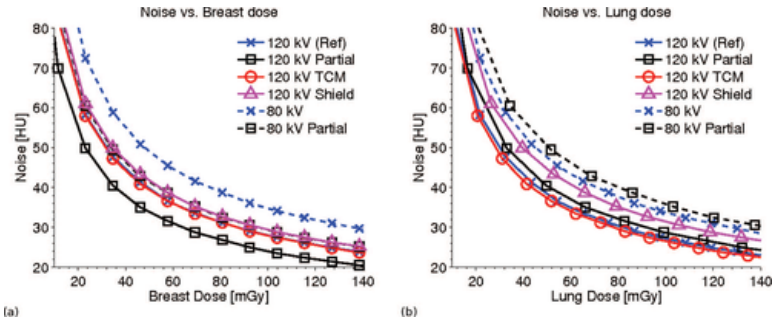

Figure 6

Noise vs (a) breast dose and (b) lung dose. Noise is measured as pixel standard deviation.

Figure 7 plots the CNR of the investigated protocols versus breast and lung dose for both tasks. The CNR curves indicate a similar relative ranking of protocol performance as the corresponding $\hat{A}_{\mathrm{FE}}$ curves.

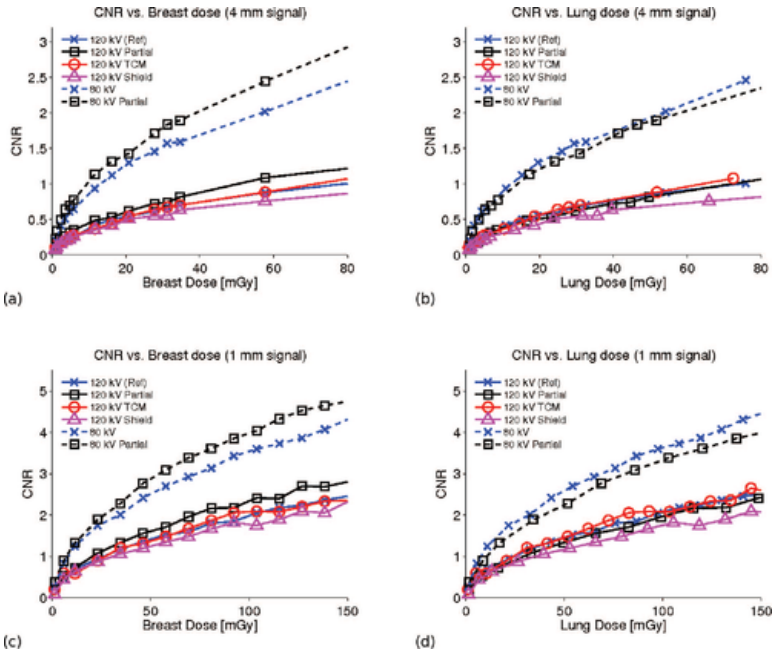

Figure 7
CNR vs (a) breast dose and (b) lung dose for the 4-mm, 3.25 mg/ml signals. CNR vs (c) breast dose and (d) lung dose for the 1-mm, 6.0 mg/ml signals.

Tables I and II list values of $\hat{A}_{\mathrm{FE}}$, CNR, contrast, noise, and lung dose for each protocol for the 4-mm, 3.25 mg/ml and 1-mm, 6.0 mg/ml task at equivalent breast dose (≈21 mGy for the 4-mm task, and ≈81 mGy for the 1-mm task). The probability of signal detection for the 80 kV and 80 kV partial protocols is virtually certain ($\hat{A}_{\mathrm{FE}} = 1.0$), with lower detectability for the other protocols. Figure 8 shows an example of a signal-present image for each protocol at equivalent breast dose for the 4-mm, 3.25 mg/ml task.

Table I. Image quality metrics and lung doses for each protocol for the 4-mm, 3.25 mg/ml task at equivalent breast dose (≈21 mGy).

Protocol	$\hat{A}_{\mathrm{FE}}$	CNR	Contrast (HU)	Noise (HU)	Lung dose (mGy)
120 kV (ref)	0.63	0.55	33.8	61.2	19.5
120 kV partial	0.84	0.62	32.5	52.4	29.7

120 kV TCM	0.67	0.54	33.3	61.2	18.6
120 kV shield	0.40	0.50	32.4	64.3	23.7
80 kV	1.00	1.30	99.3	76.4	19.5
80 kV partial	1.00	1.43	91.4	64.1	30.9

Table II. Image quality metrics and lung doses for each protocol for the 1-mm, 6.0 mg/ml task at equivalent breast dose (≈81 mGy).

Protocol	$\hat{A}_{\mathrm{FE}}$	CNR	Contrast (HU)	Noise (HU)	Lung dose (mGy)
120 kV (ref)	0.71	1.81	56.4	31.2	75.9
120 kV partial	0.80	2.17	58.2	26.9	115.7
120 kV TCM	0.71	1.87	58.4	31.2	72.5
120 kV shield	0.47	1.67	54.3	32.7	92.3
80 kV	1.00	3.13	121.5	38.8	76.6
80 kV partial	1.00	3.61	117.1	32.5	120.3

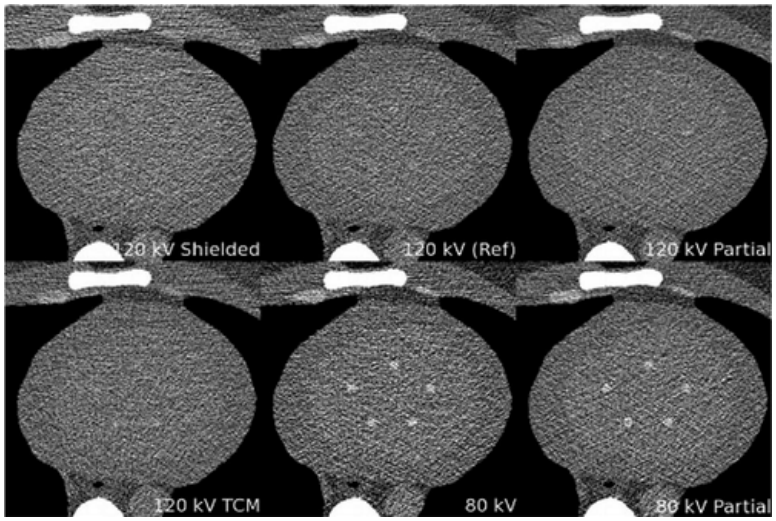

Figure 8
Example of a 4-mm, 3.25 mg/ml signal-present image for each protocol at equivalent breast dose (≈21 mGy). Window/level is 400/115 HU for the 120 kV images, and 400/280 HU for the 80 kV images.

Table III lists values of CNR, contrast, noise, breast dose, and lung dose for each protocol at an equivalent $\hat{A}_{\mathrm{FE}}$of 0.96 for the 4-mm, 3.25 mg/ml task. Figure 9(a) indicates for this task and value of $\hat{A}_{\mathrm{FE}}$that the 120 kV TCM, 120 kV partial, 80 kV, and 80 kV partial protocols reduced dose to the breast by 6.0%, 17.6%, 80.5%, and 85.3%, respectively, while the shielded protocol increased dose to the breast by 67.8%. Figure 9(b) indicates that the 120 kV partial and shielded scans increased dose to the lung by 25.3% and 103.4%, respectively, while the TCM, 80 kV, and 80 kV partial scans reduced dose to the lung by 10.4%, 80.5%, and 76.7%, respectively. At this equivalent $\hat{A}_{\mathrm{FE}}$ of 0.96, the 80 kV and 80 kV partial protocols yielded an approximate three-fold increase in both image noise (186.2% and 171.0%, respectively) and contrast (185.5% and 182.7%, respectively), while CNR across all protocols varied between a 1.4% decrease to an 8.6% increase relative to the reference protocol. An example of a signal-present image for each protocol for the 4-mm, 3.25 mg/ml task at this equivalent $\hat{A}_{\mathrm{FE}}$ of approximately 0.96 is shown in Fig. 10.

Table III. Image quality metrics and dose estimates for each protocol at approximately equivalent $\hat{A}_{\mathrm{FE}}$ (≈0.96) for the 4-mm, 3.25 mg/ml task.

Protocol	CNR	Contrast (HU)	Noise (HU)	Breast dose (mGy)	Lung dose (mGy)
120 kV (ref)	0.72	33.2	46.3	36.8	34.5
120 kV partial	0.74	31.8	43.3	30.3	43.2
120 kV TCM	0.70	33.1	47.3	34.6	30.9
120 kV shield	0.78	29.1	37.3	61.8	70.2
80 kV	0.71	94.8	132.6	7.2	6.7
80 kV partial	0.75	93.9	125.5	5.4	8.0

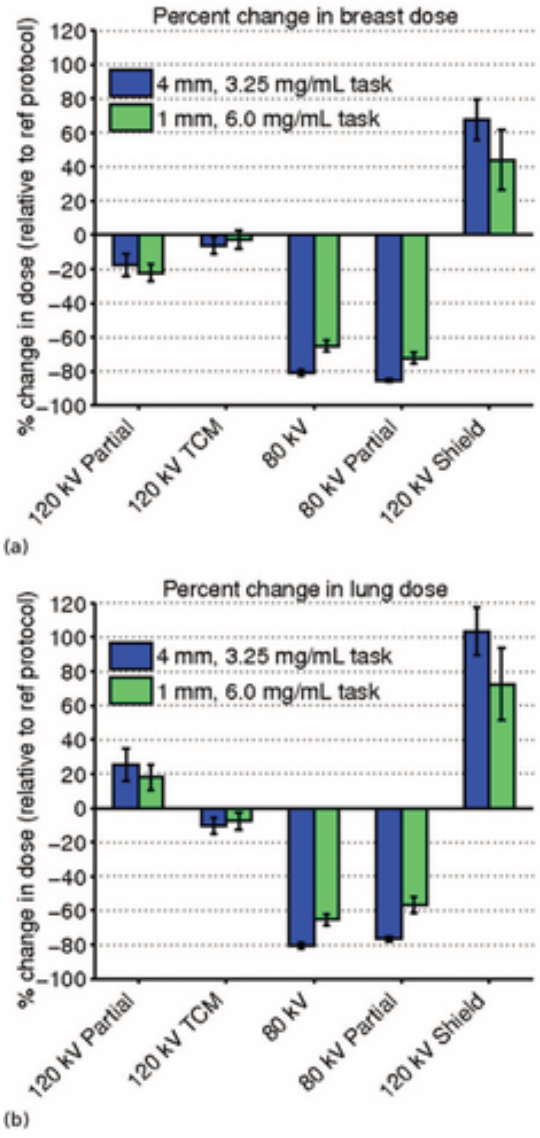

Figure 9
Percent change in (a) breast and (b) lung dose for each protocol, relative to the reference protocol, for both tasks.

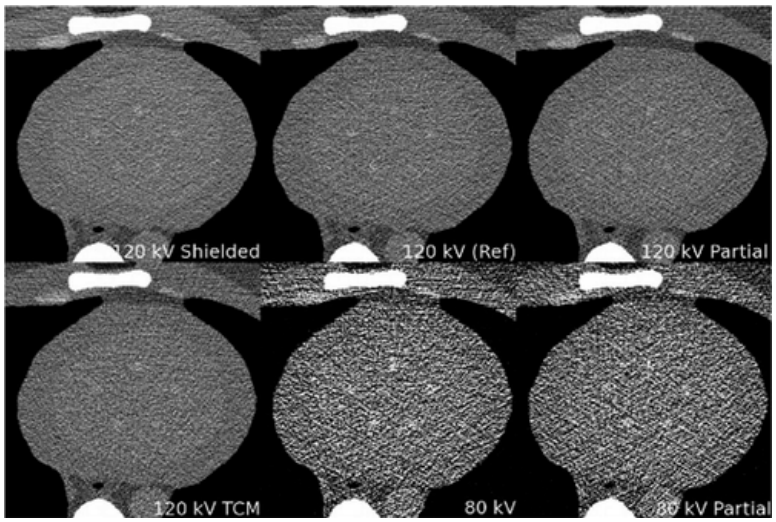

Figure 10
Example of a signal-present image for each protocol at equivalent $\hat{A}_{\mathrm{FE}}$ (≈0.96). Window/level is 400/115 HU for the 120 kV images, and 400/280 HU for the 80 kV images.

Table IV lists values of CNR, contrast, noise, breast dose, and lung dose for each protocol at an equivalent $\hat{A}_{\mathrm{FE}}$ of 0.96 for the 1-mm, 6.0 mg/ml task. Again we note that the higher dose values reported for the 1-mm, 6.0 mg/ml task (Table IV) compared to the 4-mm, 3.25 mg/ml task (Table III) are a result of the higher level of difficulty (in terms of signal detectability) of the 1-mm, 6.0 mg/ml task. Similar trends in the values reported in the tables were observed for the 1-mm task as for the 4-mm task, including dose performance, as seen in Fig. 9. However, the 80 kV and 80 kV partial protocols demonstrated higher breast and lung dose savings for the 4-mm, 3.25 mg/ml task than for the 1-mm, 6.0 mg/ml task, and the shielded protocol showed a higher increase in breast and lung dose for the 4-mm, 3.25 mg/ml task than for the 1-mm, 6.0 mg/ml task, whereas the 120 kV partial and TCM protocols demonstrated more comparable dose savings to the breast and lung across tasks.

Table IV. Image quality metrics and dose estimates for each protocol at approximately equivalent $\hat{A}_{\mathrm{FE}}$(≈0.96) for the 1-mm, 6.0 mg/ml task.

Protocol	CNR	Contrast (HU)	Noise (HU)	Breast dose (mGy)	Lung dose (mGy)
120 kV (ref)	2.45	56.3	23.0	148.9	140.4
120 kV partial	2.40	53.7	22.4	115.8	166.0
120 kV TCM	2.35	54.6	23.3	144.9	129.7
120 kV shield	2.75	56.0	20.0	214.5	242.2
80 kV	2.57	122.9	47.9	52.0	48.7
80 kV partial	2.56	116.0	45.4	41.1	60.8

IV. DISCUSSION

Overall, for the 4-mm, 3.25 mg/ml task, the 80 kV and 80 kV partial-angle protocols demonstrated the highest dose savings to the breast (80.5% and 85.3%, respectively), as well as to the lung (80.5% and 85.3%, respectively). This is due in large part to the approximate three-fold increase in contrast that resulted from the lowered kV (Table III). We also saw a nearly three-fold increase in image noise (Table III). In theory, equivalent $\hat{A}_{\mathrm{FE}}$ across protocols represents equivalent signal detectability, and thus equivalent image quality for the specified (signal detection) task. In practice, certain characteristics of the signal (e.g., size, shape, and contrast) may be unknown *a priori* or may vary. In such cases, the increased noise that would result when acquiring images with the 80 kV or 80 kV partial protocols at the dose required to achieve the reported breast dose

savings could be deemed clinically unacceptable, as it may hinder the observer's ability to detect signals with characteristics other than those presented in this study. Some dose savings may still be realizable with reduced kV protocols even if the tube-current is increased to achieve a more desirable noise level. For example, Fig. 11 displays an image produced by the 80 kV partial scan with the breast dose level indicated in Table III, as well as an image produced by the 80 kV partial scan with a breast dose level five times greater, which would yield a 26.6% reduction in breast dose, a 21.2% increase in noise, and a 132.4% increase in CNR relative to the reference protocol, and an $\hat{A}_{\mathrm{FE}}$ of 1.0.

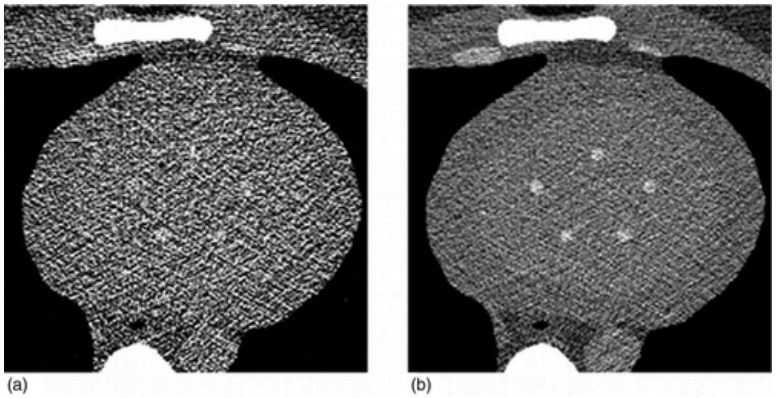

Figure 11
(a) A 4-mm, 3.25 mg/ml signal-present image using the 80 kV partial protocol with $\hat{A}_{\mathrm{FE}}\approx 0.96$ (the same image as shown in Fig. 10). This image yields 85.3% dose savings to the breast and 171.0% increase in noise relative to the reference protocol. (b) A 4-mm, 3.25 mg/ml signal-present image using the 80 kV partial protocol with five times the dose of that shown in (a), resulting in a 26.6% decrease in breast dose and 21.2% increase in noise, relative to the reference protocol, and an $\hat{A}_{\mathrm{FE}}$ of 1.0. Both images are shown at a window/level of 400/280 HU.

The TCM protocol demonstrated comparable performance to the reference protocol for both tasks. We chose an angular TCM protocol that modulates tube-current proportionally to the square root of the attenuation, which has been shown to be optimal with respect to image noise for a homogenous, elliptical phantom.36 Different manufacturers employ different angular tube-current modulation algorithms (e.g., sinusoidal vs attenuation-based), which can lead to variation in reported dose savings depending on the protocol, patient geometry, and the type of dose being reported (e.g., effective dose vs organ-specific dose).46–48 While the algorithm we chose is similar in theory to clinically available attenuation-based tube-current modulation algorithms36,47 and is optimal with respect to image noise (as measured by the pixel standard deviation), it is likely not optimal with respect to breast dose and task-based image quality (e.g., signal-detectability). It may be interesting to explore the performance of other TCM algorithms with respect to these two parameters.

The 120 kV partial protocol decreased breast dose by 17.6% for the 4-mm, 3.25 mg/ml task, but at the cost of 25.3% increased lung dose. The 120 kV partial protocol resulted in small decreases in both the noise (6.6%) and the contrast (4.3%) when maintaining equivalent $\hat{A}_{\mathrm{FE}}$ to the reference protocol (Table III). Thus, the relative increase in performance versus breast dose was mostly attributable to the lack of direct exposure of the breasts to radiation during the partial scan protocol, for which the tube-current is turned off during a 128° arc of AP projections. Similarly, the increased tube-current during PA projections caused the decreased performance versus lung dose.

We chose a 128° arc during which to turn off the tube-current for the partial-angle protocols to approximate currently available organ-based dose modulation technology.11,12,38–40 Still, in many female patients, including the phantom used in this study, a wider arc is required to fully contain the breast tissue.40 Further work is required to better determine the tradeoff between breast dose and image quality as a function of the width of the partial-angle arc for breasts of various shapes and sizes.

The 80 kV and 80 kV partial protocols showed greater reduction in breast and lung dose for the 4-mm task than for the 1-mm task, while the shielded protocol demonstrated increased breast and lung dose for the 4-mm task compared to the 1-mm task. While the 1-mm task may not be as clinically relevant for a CTCA scan (too small and high contrast), these results suggest that estimated percent changes in dose are task-dependent (Fig. 9). This highlights the importance of choosing an appropriate, clinically relevant image quality task when reporting the percent changes in dose associated with a given protocol, reconstruction method, etc.

We also note that the reported increase in breast and lung dose produced by the shielded protocol for both tasks is contrary to the original hypothesis that the breast shield may be used as a dose reduction method. Still, these results may be considered effectively consistent with studies11,12,15 that have reported dose savings to the breast at the cost of degraded image quality (e.g., increased noise). In addition, Fig. 5 suggests that globally reducing the tube-current is a more effective method of reducing breast (and lung) dose than shielding.

In general, the CNR curves indicate a similar relative ranking of protocol performance as the corresponding $\hat{A}_{\mathrm{FE}}$ curves. At an $\hat{A}_{\mathrm{FE}}$ of 0.96, the shielded protocol resulted in a 8.6% higher CNR than the 120 kV reference protocol for the 4-mm task (Table III). If the CNR of the shielded protocol was adjusted to match that of the reference protocol, the shielded protocol would increase breast and lung dose by 42.2% and 72.4%, respectively, compared to the reference scan. In comparison, when both protocols maintained equivalent $\hat{A}_{\mathrm{FE}}$ of 0.96, the shielded protocol increased breast and lung dose by 67.8% and 103.4%, respectively. A similar higher CNR for the shielded protocol relative to the reference protocol was observed for the 1-mm task (12.3%). CNR can be considered an incomplete metric in the sense that it does not account for noise correlations or image artifacts. For example, two signal-present images in which all properties are the same except for differing noise correlations can be shown to have the same CNR.49 Unlike CNR, $\hat{A}_{\mathrm{FE}}$ is a task-based metric, and both noise correlations and image artifacts affect its performance. Although it is not obviously visually apparent from Fig. 8 or Fig. 10, it is possible that the streaking commonly associated with the use of shields10–12,15 altered the noise correlations in such a way as to result in an 8.6% (4-mm task) and 12.3% (1-mm task) increase in CNR at equivalent $\hat{A}_{\mathrm{FE}}$ compared to the reference protocol. For all other cases, the CNR varied by less than 5.0% across all protocols in images with an $\hat{A}_{\mathrm{FE}}$ of 0.96, and so $\hat{A}_{\mathrm{FE}}$ and CNR resulted in similar estimates of dose performance (within 8.5% of one another) for these cases.

Clinically, it is common to use a breast shield in conjunction with a TCM protocol. In such cases, the shield should be placed on top of the patient *after* acquisition of the CT radiograph that is used in estimating the modulation scheme.11 Thus, while we did not model this combined protocol, we would not expect to see results much different from those of the shielded protocol due to the fact that our TCM protocol showed little deviation in performance from the reference protocol and the relative modulation at each angle for a shielded TCM protocol would be no different than that of the simulated nonshielded TCM protocol.

Although there are differences in signal detectability performance for the 4 and 1-mm signal-size tasks, as shown in Figs. 5 and 9, the plots show similar trends. This indicates a robustness of $\hat{A}_{\mathrm{FE}}$ with regard to the particular task being investigated.

There are several advantages in using a signal detectability metric for signals at unknown locations compared with SNR calculations obtained for fixed signals with various other model observers (ideal, Hotelling, channelized Hotelling, nonprewhitening, etc.). The unknown-signal-location metrics compare the signal realizations with the extreme occurrences of false signal-like features that randomly occur in the background due to noise. On the other hand, the SNR metrics derived for known signal locations compare signal realizations with the fluctuations of a fixed signal-sized patch of image background, where extreme values are much less likely to occur and hence much less likely to be confounded with a signal. Therefore, the metrics derived for unknown signal locations are more sensitive to differences in noise levels and/or noise patterns. In addition, unlike the fixed signal location

metrics, unknown-signal-location metrics take into account the clinically relevant case of correctly identifying the signal location.

By using nonparametric methods to estimate A_{FE}, we avoid the reliance on any specific models of or assumptions about the data. Further, while the calculation of ideal and quasi-ideal observer SNRs can require several hundreds or even thousands of signal-present and signal-absent images, which can be difficult to obtain experimentally, the nonparametric estimator, $\hat{A}_{\mathrm{FE}}$, can be calculated with fairly low statistical uncertainty using relatively few image samples (on the order of tens).

There are some limitations of our methods. First, it is important to note that the reported dose and image quality estimates, and thus the reported percent changes in dose for each protocol, are specific to our simulation geometry, patient size, and reconstruction algorithm. For example, the noise increase quantified for the 80 kV protocols is expected to increase with patient size. In addition, we used the same reconstruction algorithm for each protocol, however, it is unlikely that this algorithm (e.g., reconstruction kernel) was optimal across all protocols. Thus, additional work is required to study task-based detectability over a range of patient sizes, as well as to determine how the performance of such protocols may change when protocol-specific reconstruction kernels are used.

Second, our analytical ray-tracing algorithm did not model x-ray scatter. In the presence of scatter, we would expect to see streaking artifacts, CT number inaccuracies, and a decrease in the CNR (Refs. 50,51) for all protocols. Postpatient collimation and software algorithms on clinical CT systems provide some correction of scatter-induced degradations of image quality. We do not expect the relative trends in our results to change considerably if scatter were simulated along with appropriate scatter-correction techniques. One case in which scatter could potentially degrade performance relative to the other protocols is the shielded protocol. This is due to the fact that the shield itself is expected to generate scattered photons that may deteriorate image quality. Further, these back-scattered photons may also increase breast dose.

Third, we note that our model for CTCA does not account for cardiac protocols that use prospective or retrospective gating techniques. Instead, we chose to model 320-detector row CT, whose ability to reduce dose during CTCA protocols has been previously demonstrated.33 Further, while some of the protocols we have modeled may not typically be employed during cardiac CT, they are often used during chest CT, for which the signal detectability metric used in this study may still be used to evaluate image quality.

V. CONCLUSION

This simulation study compared the dose performance and task-based signal detection and localization performance of several CT protocols intended to reduce breast dose. Localization and detectability was quantified with the $\hat{A}_{\mathrm{FE}}$ metric using tens of image samples for each protocol. The 80 kV and 80 kV partial-angle protocols demonstrated the greatest reduction to breast and lung dose. However, in clinical applications, due to the more complex nature of the tasks, the subsequent increase in image noise may be considered too large. In these situations, tube output for these protocols can be adjusted to achieve a more desirable noise level at a lesser reduction in dose. Contrary to our original hypothesis, breast shielding increased breast and lung dose when maintaining equivalent $\hat{A}_{\mathrm{FE}}$. We have demonstrated that CNR may not be a reliable metric of signal detectability as it does not account for noise correlations or image artifacts. Finally, the results demonstrated that comparisons of dose performance depend on both the image quality metric and the specific task.

ACKNOWLEDGMENTS

This study was supported in part by an appointment to the Research Participation Program at the FDA Center for Devices and Radiological Health administered by the Oak Ridge Institute for Science and Education through an interagency agreement between the United States Department of Energy and the Food and Drug

Administration, Office of Women's Health. Computer simulations were performed on the Marquette University Pere High Performance Computing Cluster, which was funded in part by National Science Foundation Award Nos. OCI-0923037 and CBET-0521602. The authors would like to thank Lars E. Olson, Ph.D. and David Herzfeld for their support with the high performance cluster.

REFERENCES

1. Smith-Bindman, R., " Is computed tomography safe?," *N. Engl. J. Med.* 363(1), 1– 4 (2010).10.1056/NEJMp1002530
2. Feinendegen, L. E., " Evidence for beneficial low level radiation effects and radiation hormesis," *Br. J. Radiol.* 78, 3– 7 (2005).10.1259/bjr/63353075
3. Neumaier, T., Swenson, J., Pham, C., Polyzos, A., Lo, A. T., Yang, P., Dyball, J., Asaithamby, A., Chen, D. J., and Bissell, M. J., " Evidence for formation of DNA repair centers and dose-response nonlinearity in human cells," *Proc. Natl. Acad. Sci. U.S.A.* 109(2), 443– 448 (2012).10.1073/pnas.1117849108
4. National Council on Radiation Protection and Measurements, " Evaluation of the linear-nonthreshold dose-response model for ionizing radiation," NCRP Report No. 136 (NCRP, Bethesda, MD, 2001).
5. Committee to Assess Health Risks from Exposure to Low Levels of Ionizing Radiation, Board on Radiation Effects Research, Division of Earth and Life Sciences, and National Research Council of The National Academies, Health Risks from Exposure to Low Levels of Ionizing Radiation: BEIR VII Phase 2 (The National Academies, Washington, DC, 2006).
6. Pearce, M. S., Salotti, J. A., Little, M. P., McHugh, K., Lee, C., Kim, K.-P., Howe, N. L., Ronckers, C. M., Rajaraman, P., Craft, A. W., Parker, L., and Berrington de Gonzalez, A., " Radiation exposure from CT scans in childhood and subsequent risk of leukaemia and brain tumours: A retrospective cohort study," *Lancet* 38(9840), 499– 505 (2012).
7. Einstein, A. J., Henzlova, M. J., and Rajagopalan, S., " Estimating risk of cancer associated with radiation exposure from 64-slice computed tomography coronary angiography," *J. Am. Med. Assoc.* 298(3), 317– 323 (2007).10.1001/jama.298.3.317
8. Smith-Bindman, R., Lipson, J., Marcus, R., Kim, K.-P., Mahesh, M., Gould, R., Berrington de Gonzalez, A., and Miglioretti, D. L., " Radiation dose associated with common computed tomography examinations and the associated lifetime attributable risk of cancer," *Arch. Intern. Med.* 169(22), 2078– 2086 (2009).10.1001/archinternmed.2009.427
9. International Commission on Radiological Protection, " The 2007 Recommendations of the International Commission on Radiological Protection," ICRP Publication 103 (International Commission on Radiological Protection, Essen, 2007).
10. Hurwitz, L. M., Yoshizumi, T. T., Goodman, P. C., Nelson, R. C., Toncheva, G., Nguyen, G. B., Lowry, C., and Anderson-Evans, C., " Radiation dose savings for adult pulmonary embolus 64-MDCT using bismuth breast shields, lower peak kilovoltage, and automatic tube current modulation," *Am. J. Roentgenol.* 192(1), 244– 253 (2009).10.2214/AJR.08.1066
11. Wang, J., Duan, X., Christner, J. A., Leng, S., Yu, L., and McCollough, C. H., " Radiation dose reduction to the breast in thoracic CT: Comparison of bismuth shielding, organ-based tube current modulation, and use of a globally decreased tube current," *Med. Phys.* 38(11), 6084– 6092 (2011).10.1118/1.3651489
12. Vollmar, S. V. and Kalender, W. A., " Reduction of dose to the female breast in thoracic CT: A comparison of standard-protocol, bismuth-shielded, partial and tube-current-modulated CT examinations," *Eur. Radiol.* 18(8), 1674– 1682 (2008).10.1007/s00330-008-0934-9
13. Angel, E., Yaghmai, N., Jude, C. M., Demarco, J. J., Cagnon, C. H., Goldin, J. G., Primak, A. N., Stevens, D. M., Cody, D. D., McCollough, C. H., and McNitt-Gray, M. F., " Monte Carlo simulations to assess the effects of tube current modulation on breast dose for multidetector CT," *Phys. Med. Biol.* 54(3), 497– 512 (2009).10.1088/0031-9155/54/3/003
14. Vollmar, S. V. and Kalender, W. A., " Reduction of dose to the female breast as a result of spectral optimisation for high-contrast thoracic CT imaging: A phantom study," *Br. J. Radiol.* 82, 920– 929 (2009).10.1259/bjr/28017710

15. Geleijns, J., Salvado Artells, M., Veldkamp, W. J. H., López Tortosa, M., and Calzado Cantera, A., " Quantitative assessment of selective in-plane shielding of tissues in computed tomography through evaluation of absorbed dose and image quality," *Eur. Radiol.* 16(10), 2334– 2340 (2006).10.1007/s00330-006-0217-2
16. Hopper, K. D., King, S. H., Lobell, M. E., TenHave, T. R., and Weaver, J. S., " The breast: In-plane x-ray protection during diagnostic thoracic CT—Shielding with bismuth radioprotective garments," *Radiology* 205(3), 853– 858 (1997).
17. Fricke, B. L., Donnelly, L. F., Frush, D. P., Yoshizumi, T., Varchena, V., Poe, S. A., and Lucaya, J., " In-plane bismuth breast shields for pediatric CT: Effects on radiation dose and image quality using experimental and clinical data," *Am. J. Roentgenol.* 180, 407– 411 (2003).10.2214/ajr.180.2.1800407
18. International Commission on Radiation Units and Measurements, " Medical imaging—The assessment of image quality," ICRU Report No. 54 (ICRU Publications, Washington, DC, 1996).
19. Barrett, H. H., " Objective assessment of image quality: Effects of quantum noise and object variability," *J. Opt. Soc. Am. A* 7(7), 1266– 1278 (1990).10.1364/JOSAA.7.001266
20. Swensson, R. G., " Unified measurement of observer performance in detecting and localizing target objects on images," *Med. Phys.* 23, 1709– 1725 (1996).10.1118/1.597758
21. Popescu, L. M., " Nonparametric signal detectability evaluation using an exponential transformation of the FROC curve," *Med. Phys.* 38(10), 5690– 5702 (2011).10.1118/1.3633938
22. Leng, S., Yu, L., Chen, L., Giraldo, J. C. R., and McCollough, C. H., " Correlation between model observer and human observer performance in CT imaging when lesion location is uncertain," *Proc. SPIE* 8313, 83131M, (2012).10.1117/12.912126
23. Popescu, L. M. and Myers, K. J., " CT image assessment by low contrast signal detectability evaluation with unknown signal location," in The Second International Conference on Image Formation in X-Ray Computed Tomography, Salt Lake City, Utah, 2012.
24. Popescu, L. M. and Lewitt, R. M., " Small nodule detectability evaluation using a generalized scan-statistic model," *Phys. Med. Biol.* 51, 6225– 6244 (2006).10.1088/0031-9155/51/23/020
25. Badal, A., " penEasy Imaging software extension to penEasy" (2010) (available URL: http://code.google.com/p/peneasy-imaging).
26. Sempau, J., " penEasy software" (2010) (available URL: http://inte.upc.edu/downloads).
27. Salvat, F., Fernández-Varea, J., and Sempau, J., " PENELOPE-2006: A code system for Monte Carlo simulation of electron and photon transport," in Workshop Proceedings (Nuclear Energy Agency, Organization for Economic Co-operation and Development, Barcelona, Spain, 2006).
28. Christ, A., Kainz, W., Hahn, E. G., Honegger, K., Zefferer, M., Neufeld, E., Rascher, W., Janka, R., Bautz, W., Chen, J., Kiefer, B., Schmitt, P., Hollenbach, H.-P., Shen, J., Oberle, M., Szczerba, D., Kam, A., Guag, J. W., and Kuster, N., " The virtual family—Development of surface-based anatomical models of two adults and two children for dosimetric simulations," *Phys. Med. Biol.* 55(2), N23– N38 (2010).10.1088/0031-9155/55/2/N01
29. Gu, S., Gupta, R., and Kyprianou, I., " Computational high-resolution heart phantoms for medical imaging and dosimetry simulations," *Phys. Med. Biol.* 56(18), 5845– 5864 (2011).10.1088/0031-9155/56/18/005
30. International Commission on Radiological Protection, " Adult Reference Computational Phantoms," ICRP Publication 110 (International Commission on Radiological Protection, Essen, 2009).
31. Woodard, H. and White, D., " The composition of body tissues," *Br. J. Radiol.* 59(708), 1209– 1219 (1986).10.1259/0007-1285-59-708-1209
32. Cristy, M. and Eckerman, K. F., " Specific absorbed fractions of energy at various ages from internal photon sources," ORNL Report No. TM-8381 (Oak Ridge National Laboratory, Oak Ridge, TN, 1987), Vols. I–VII.
33. Einstein, A. J., Elliston, C. D., Arai, A. E., Chen, M. Y., Mather, R., Pearson, G. D. N., DeLaPaz, R. L., Nickoloff, E., Dutta, A., and Brenner, D. J., " Radiation dose from single-heartbeat coronary CT angiography performed with a 320-detector row volume scanner," *Radiology* 254(3), 698– 706 (2010).10.1148/radiol.09090779

34. Salomon, E. J., Barfett, J., Willems, P. W. A., Geibprasert, S., Bacigaluppi, S., and Krings, T., " Dynamic CT angiography and CT perfusion employing a 320-detector row CT," *Clin. Neuroradiol.* 19(3), 187– 196 (2009).10.1007/s00062-009-9019-7
35. McKenney, S. E., Nosratieh, A., Gelskey, D., Yang, K., Huang, S.-Y., Chen, L., and Boone, J. M., " Experimental validation of a method characterizing bow tie filters in CT scanners using a real-time dose probe," *Med. Phys.* 38(3), 1406– 1415 (2011).10.1118/1.3551990
36. Gies, M., Kalender, W. A., Wolf, H., Suess, C., and Madsen, M. T., " Dose reduction in CT by anatomically adapted tube current modulation. I. Simulation studies," *Med. Phys.* 26(11), 2235– 2257 (1999).10.1118/1.598779
37. Cranley, K., Gilmore, B., Fogarty, G. W. A., and Desponds, L., " Catalogue of diagnostic X-ray spectra and other data," IPEM Report No. 78 (The Institute of Physics and Engineering in Medicine (IPEM), 1997).
38. Duan, X., Wang, J., Christner, J. A., Leng, S., Grant, K. L., and McCollough, C. H., " Dose reduction to anterior surfaces with organ-based tube-current modulation: Evaluation of performance in a phantom study," *Am. J. Roentgenol.* 197, 689– 695 (2011).10.2214/AJR.10.6061
39. Wang, J., Duan, X., Christner, J. A., Leng, S., Grant, K. L., and McCollough, C. H., " Bismuth shielding, organ-based tube current modulation, and global reduction of tube current for dose reduction to the eye at head CT," *Radiology* 262(1), 191– 198 (2012).10.1148/radiol.11110470
40. Lungren, M. P., Yoshizumi, T. T., Brady, S. M., Toncheva, G., Anderson-Evans, C., Lowry, C., Zhou, X. R., Frush, D., and Hurwitz, L. M., " Radiation dose estimations to the thorax using organ-based dose modulation," *Am. J. Roentgenol.* 199, W65– W73 (2012).10.2214/AJR.11.7798
41. Rupcich, F., Badal, A., Kyprianou, I., and Schmidt, T. G., " A database for estimating organ dose for coronary angiography and brain perfusion CT scans for arbitrary spectra and angular tube current modulation," *Med. Phys.* 39(9), 5336– 5346 (2012).10.1118/1.4739243
42. Parker, D. L., " Optimal short scan convolution reconstruction for fan beam CT," *Med. Phys.* 9(2), 254– 257 (1982).10.1118/1.595078
43. Hsieh, J., Computed Tomography: Principles, Design, Artifacts, and Recent Advances (SPIE, Bellingham, WA, 2003).
44. Hoffmann, M. H. K., Shi, H., Schmitz, B. L., Schmid, F. T., Lieberknecht, M., Schulze, R., Ludwig, B., Kroschel, U., Jahnke, N., Haerer, W., Brambs, H. J., and Aschoff, A. J., " Noninvasive coronary angiography with multislice computed tomography," *J. Am. Med. Assoc.* 293(20), 2471– 2478 (2005).10.1001/jama.293.20.2471
45. Davies, H. E., Wathen, C. G., and Gleeson, F. V., " Risks of exposure to radiological imaging and how to minimise them," *Br. Med. J.* 342, 589– 593 (2011).10.1136/bmj.d947
46. McCollough, C. H., Bruesewitz, M. R., and Kofler, J. M., " CT dose reduction and dose management tools: Overview of available options," *Radiographics* 26, 503– 512 (2006).10.1148/rg.262055138
47. Kalra, M. K., Maher, M. M., Toth, T. L., Schmidt, B., Westerman, B. L., Morgan, H. T., and Saini, S., " Techniques and applications of automatic tube current modulation for CT," *Radiology* 233, 649– 657 (2004).10.1148/radiol.2333031150
48. Lee, C. H., Goo, J. M., Ye, H. J., Ye, S. J., Park, C. M., Chun, E. J., and Im, J. G., " Radiation dose modulation techniques in the multidetector CT Era: From basics to practice1," *Radiographics* 28, 1451– 1459 (2008).10.1148/rg.285075075
49. Boedeker, K. and McNitt-Gray, M., " Application of the noise power spectrum in modern diagnostic MDCT: Part II. Noise power spectra and signal to noise," *Phys. Med. Biol.* 52, 4027– 4046 (2007).10.1088/0031-9155/52/14/002
50. Siewerdsen, J. H. and Jaffray, D. A., " Cone-beam computed tomography with a flat-panel imager: Magnitude and effects of x-ray scatter," *Med. Phys.* 28, 220– 231 (2001).10.1118/1.1339879
51. Joseph, P. M. and Spital, R. D., " The effects of scatter in x-ray computed tomography," *Med. Phys.* 9, 464– 472 (1982).10.1118/1.595111